Opt Quant Electron manuscript No.
(will be inserted by the editor)

Theoretical and numerical modeling of linear and nonlinear propagation in graphene waveguides

Alexandros Pitilakis · **Dimitrios Chatzidimitriou** · **Emmanouil E. Kriezis**

Received: date / Accepted: date

Abstract A formulation for the theoretical and numerical modeling of electromagnetic wave propagation in graphene-comprising waveguides is presented, targeting applications in the linear and nonlinear regime. Waveguide eigenmodes are rigorously calculated using the finite-element method (FEM) in the linear regime and are subsequently used to extract nonlinear properties in terms of the nonlinear Schrödinger equation framework. Graphene sheets are naturally represented as sheet/2D media and are seamlessly implemented with interface conditions in the FEM, thus greatly enhancing the computational efficiency. This formulation is used to analyze the nonlinear performance of several graphene-comprising waveguide configurations in the optical band, including silicon-based photonic waveguides, metal-based plasmonic waveguides and glass microfibers. Optimal design choices are identified for each configuration and subtle aspects of the FEM-based modeling, especially important for plasmonic waveguides, are highlighted.

Keywords Graphene · Optical waveguides · Nonlinear waveguides · Finite element method · Mode solver · Photonic waveguides · Plasmonic waveguides · Microfiber

PACS 42.25.Bs · 42.65.-k · 42.65.Wi · 42.65.Hw · 42.82.-m · 71.36.+c · 78.67.Wj

1 Introduction

Graphene is a 2D material that has attracted considerable attention in many research fields due to its unique properties (Geim and Novoselov 2007; Novoselov et al 2012). Specifically, one of the most interesting features for photonic and optoelectronic applications is the tunable conductivity of graphene, achieved by controlling its Fermi level (also called chemical potential) by electrical gating (Vakil and Engheta 2011) or by strong magnetic fields. Various optical devices based on graphene have been theoretically and experimentally investigated, including photodetectors (Xia et al 2009), modulators (Liu et al 2011, 2012), mode locked lasers (Sun et al 2010) and polarizers (Bao et al 2011). Recently, the experimental evidence

A. Pitilakis · D. Chatzidimitriou · E. E. Kriezis
Department of Electrical and Computer Engineering, Aristotle University of Thessaloniki, Thessaloniki GR-54125, Greece
Tel.: +30-2310-996362, Fax: +30-2310-996312
E-mail: alexpiti@auth.gr

of strong nonlinear response from graphene (Hendry et al 2010) led to considerable efforts for the realization of a new generation of practical nonlinear photonic guided-wave devices for all optical applications (Zhang et al 2012; Wu et al 2014). Despite the ensuing first-principle theoretic predictions that toned down the initial expectations (Khurgin 2014), the interest in this research field remains intense while the convergence between experiment and theory is pending.

In this work we present a rigorous framework for the numerical modeling of graphene-comprising nanophotonic waveguides (Xia et al 2014) both in the linear regime, using a Finite Element Method (FEM) (Volakis et al 1998) implementation, and in the nonlinear regime, in terms of the so called nonlinear Schrödinger equations (NLSE) (Agrawal 2007). A more generic formalism is outlined in (Boardman et al 2007; Rapoport and Grimalsky 2011; Rapoport 2014), called the method of nonlinear evolution equations in layered structures (NEELS), which can alternatively be used to model wave propagation in structures with arbitrary nonlinear sheet and bulk materials including bi-anisotropic layered metamaterials, gyrotropic media, plasma, 2D electron gas (graphene) etc. In recent literature, graphene is commonly implemented as an equivalent (or effective) isotropic bulk medium layer of sub-nanometer thickness (Vakil and Engheta 2011). Using the FEM, this implementation usually leads to considerable memory requirements, especially for modeling of 3D structures. This equivalent bulk-medium representation may yield correct results if properly implemented, for instance using equivalent anisotropic susceptibility tensors, but it is usually proven suboptimal as it treats an atom-thick material in a bulk fashion (Chatzidimitriou et al 2015). Therefore, we propose modeling two-dimensional materials like graphene as infinitesimally thin sheets. Not only is this route more computationally efficient but, from a physical perspective, it more naturally encapsulates the 2D nature of sheet materials, taking fully into account their tensorial nature and the vector properties of the electromagnetic fields.

Graphene exhibits high nonlinear response (Hendry et al 2010), an essential ingredient for all optical signal processing, which along with its thermal conductivity, mechanical strength and compact nature can be used to design ultra-low footprint nonlinear photonic devices. The main goal of this work is to study the propagation of bound electromagnetic waves in waveguides comprising both bulk and sheet nonlinear materials. To this end, we rigorously calculate the eigenmodes of these waveguides in the linear regime and subsequently use them to extract the corresponding nonlinear parameters, γ_{NL} $[\mathrm{m}^{-1}\mathrm{W}^{-1}]$, that quantify their nonlinearity. For multimode waveguides or wavelength-division multiplexed (WDM) signals, a set of nonlinear parameters can be extracted, leading to set of coupled NLSE equations describing the propagation of multiple modes or signals, respectively (Pitilakis and Kriezis 2013). The nonlinear properties of sheet/2D materials like graphene are described by a nonlinear surface conductivity, similarly to how nonlinear susceptibility is used for bulk/3D materials. We show that the nonlinear parameter γ_{NL} can be eventually split into two distinct contributions: γ_b and γ_s, for bulk and sheet materials, respectively. The formulas presented here correspond to third-order self-acting phenomena only, namely the optical Kerr effect and the two-photon absorption (TPA). Nevertheless, the procedure described is generic and can be extended to narrowband third-order phenomena such as four-wave mixing (FWM) or to nonlinear processes of any order, such as second- or third-harmonic generation, within the limits of our approximations. Furthermore, the same framework can be directly used for modeling nonlinear propagation in graphene waveguides operated in the Terahertz spectral region which support surface-plasmon polariton (SPP) modes (Nikitin et al 2011; Bludov et al 2013). Finally, our formalism is used in this work to study several types of graphene-comprising optical waveguides (silicon waveguides, plasmonic waveg-

uides and glass microfibers) in order to assess their nonlinear performance and identify optimal configurations.

This paper is organized as follows: Section 2 contains the electromagnetic modeling of graphene as a conductive sheet material; we discuss how graphene is introduced in Maxwell's curl equations in the absence of nonlinearity, we outline the electromagnetic properties of graphene, we present a complete implementation of 3D-FEM modeling of structures containing both sheet and bulk media and, finally, we construct a set of coupled NLSE equations to describe nonlinear pulse propagation in multimode waveguides. Section 3 presents a numerical investigation of the overall nonlinear performance of photonic and plasmonic waveguide configurations with the addition of a graphene monolayer. Specifically, we study the impact of graphene placement on the ohmic losses and third-order nonlinear response in the following waveguide configurations: silicon wire, silicon slot, metal stripe, metal slot and glass microfiber. The conclusions of the paper follow in Section 4.

2 Theoretical and numerical formulation

2.1 Maxwell modeling of conductive sheet materials

Under the $\exp(-i\omega t)$ time harmonic convention, we can write Maxwell's frequency-domain curl equations as

$$\nabla \times \tilde{\mathbf{E}} = +i\omega\mu_0\bar{\mu}_\mathrm{r}\tilde{\mathbf{H}}, \tag{1a}$$

$$\nabla \times \tilde{\mathbf{H}} = -i\omega(\varepsilon_0\tilde{\mathbf{E}} + \tilde{\mathbf{P}}) + \tilde{\mathbf{J}}, \tag{1b}$$

where $\tilde{\mathbf{P}}$ and $\tilde{\mathbf{J}}$ are the electric polarization and current density, respectively, and the bar (as in $\bar{\mu}$) denotes a tensor in $\mathbb{R}^3$. If we do not consider any nonlinearity, the polarization can be written as $\tilde{\mathbf{P}} = \varepsilon_0\bar{\chi}^{(1)}\tilde{\mathbf{E}}$, where $\bar{\chi}^{(1)} = \bar{\varepsilon}_\mathrm{r} - I_3$ is a second-rank tensor representing the linear susceptibility and I_3 is the identity 3×3 matrix. In waveguides comprising only isotropic media, the tensor $\bar{\varepsilon}_\mathrm{r}$ degenerates to a scalar value, i.e. $\varepsilon_\mathrm{r} I_3$; similarly, $\bar{\mu}_\mathrm{r} = I_3$, as optical materials typically do not exhibit magnetic properties. In the presence of conducting bulk and sheet materials, like graphene, we can write the overall current density as a summation of their discreet contributions $\mathbf{J} = \mathbf{J}_b + \mathbf{J}_s\delta_s(\mathbf{r})$, where δ_s is an appropriate surface Dirac function (Onural 2006) describing a surface, while $\mathbf{J}_b$ and $\mathbf{J}_s$ are bulk and surface current densities, in units of $[\mathrm{A/m^2}]$ and $[\mathrm{A/m}]$, respectively. Both current densities can in turn be expressed by Ohm's law, $\mathbf{J} = \sigma\mathbf{E}$, using the appropriate conductivity tensor which corresponds to bulk or sheet materials. Furthermore, we can expand the current density into a power series in the time-domain fields

$$\mathbf{J}_b = \bar{\sigma}^{(1)}|\mathbf{E} + \bar{\sigma}^{(2)}|\mathbf{EE} + \bar{\sigma}^{(3)}|\mathbf{EEE} + \ldots, \tag{2}$$

$$\mathbf{J}_s = \bar{\sigma}_s^{(1)}|\mathbf{E} + \bar{\sigma}_s^{(2)}|\mathbf{EE} + \bar{\sigma}_s^{(3)}|\mathbf{EEE} + \ldots \tag{3}$$

where $\bar{\sigma}^{(n)}$ (bulk) and $\bar{\sigma}_s^{(n)}$ (surface) are complex-valued $(n+1)$-rank conductivity tensors (in units of $[(\mathrm{S/m})(\mathrm{m/V})^{n-1}]$ and $[\mathrm{S(m/V)}^{n-1}]$, respectively) analogous to the susceptibility tensors $\bar{\chi}^{(n)}$. The first term of Eq. (2) and (3) is the linear contribution while the rest are nonlinear contributions of increasing order. Without loss of generality, bulk-medium conductivities can be introduced as an imaginary part to the susceptibility tensor of respective rank and thus $\mathbf{J}_b$ is usually absorbed by $\mathbf{P}$ in Eq. (1b).

By default, incorporating 2D sheet materials in a vectorial $\mathbb{R}^3$ formulation requires for anisotropy considerations (Chatzidimitriou et al 2015) since the surface current density $\mathbf{J}_s$ cannot have a component normal to the sheet surface. This important feature is contained in the surface conductivity tensors, $\bar{\bar{\sigma}}_s^{(n)}$, which are treated similarly to $\bar{\bar{\chi}}^{(n)}$ and $\bar{\bar{\sigma}}^{(n)}$. Specifically, the full form of the arbitrarily oriented linear surface conductivity tensor $\bar{\bar{\sigma}}_s^{(1)}$ should be calculated using a rotation from the reference coordinate system where the sheet material tensor is typically expressed, $\bar{\bar{\sigma}}_{s,\mathrm{ref}}^{(1)}$. This is especially important when attributing surface conductivity tensors to curved (non-planar) geometries. The rotation is carried out by the matrix-multiplication formula

$$\bar{\bar{\sigma}}_s^{(1)} = R\ \bar{\bar{\sigma}}_{s,\mathrm{ref}}^{(1)}\ R^T, \tag{4}$$

where the superscript T denotes a matrix transpose. The rotation matrix R is a real-valued 3×3 array whose elements are direction cosines, defined by the angles between the corresponding axes of the reference and the rotated (actual) coordinate systems. For the rotation of the nonlinear fourth-rank conductivity tensor, a generalized expression (Butcher and Cotter 1990) is employed

$$\sigma_{s,jklm}^{(3)} = \sum_{abcd}^{xyz} R_{ja}R_{kb}R_{lc}R_{md}\ \sigma_{s,abcd,\mathrm{ref}}^{(3)}, \tag{5}$$

involving multiple summation over the indices $\{a,b,c,d\}$ that correspond to the cartesian axes $\{x,y,z\}$ of the reference coordinate system. R_{pq} is a scalar value, referring to the pq-element of the rotation matrix R. The very same procedure can be employed to calculate the rotation of anisotropic linear and nonlinear susceptibility tensors, $\bar{\bar{\chi}}^{(n)}$, for instance when a waveguide is fabricated along an arbitrary direction of a silicon crystal characterized by nonlinear anisotropy $\rho \neq 1$ (Daniel and Agrawal 2010).

Assuming that sheet media are typically positioned between bulk media, the interface boundary conditions for the electric and magnetic fields are

$$\mathbf{n}\times(\tilde{\mathbf{E}}_2 - \tilde{\mathbf{E}}_1) = \mathbf{0}, \tag{6a}$$

$$\mathbf{n}\times(\tilde{\mathbf{H}}_2 - \tilde{\mathbf{H}}_1) = \tilde{\mathbf{J}}_s, \tag{6b}$$

where $\mathbf{n}$ is the vector normal to the interface, with direction from medium 1 to medium 2. $\tilde{\mathbf{J}}_s$ is the surface current density which depends on the surface conductivity of the sheet medium that occupies the interface. In the absence of a sheet media at the interface between two bulk media, the RHS of Eq. (6b) vanishes, which enforces the continuity of the tangential component of the H-field.

2.2 Electromagnetic properties of graphene

Due to its sheet nature, the linear surface conductivity tensor of graphene in its reference orientation, i.e., in the 2D-crystal coordinate system, can only have up to four non-zero elements. This stems from the fact that graphene cannot interact with the E-field component that is normal to its surface. For example, a sheet normal to the x-axis would be described by the surface conductivity tensor

$$\bar{\bar{\sigma}}_s^{(1)} = \begin{bmatrix} 0 & 0 & 0 \\ 0 & \sigma_{s,yy} & \sigma_{s,yz} \\ 0 & \sigma_{s,zy} & \sigma_{s,zz} \end{bmatrix}, \tag{7}$$

assuming that *xyz* matches the crystal coordinate system. Additionally, in this work we assume that there are no strong magnetic fields present that would give rise to the local Hall effect (Bludov et al 2013; Stauber et al 2008) and, as a result, the off-diagonal elements of Eq. (7) are zero. Moreover, if we also take into account the symmetry of graphene lattice stating that the elements on the main diagonal of Eq. (7) are equal, we can then express the surface current as

$$\tilde{\mathbf{J}}_s = \bar{\sigma}_s^{(1)}\,\tilde{\mathbf{E}} = \sigma_c\,\tilde{\mathbf{E}}_{\parallel}, \tag{8}$$

where we replaced the general tensor expression of the linear conductivity with a scalar complex surface conductivity (σ_c in Siemens) which only interacts with the E-field components tangential to graphene, $\tilde{\mathbf{E}}_{\parallel} = \mathbf{n}\times(\tilde{\mathbf{E}}\times\mathbf{n})$, where $\mathbf{n}$ is the outwards-pointing normal vector of the graphene sheet. Equation (8) holds for any orientation ($\mathbf{n}$) of a graphene sheet that can be described by a single surface conductivity value (σ_c).

Starting with the linear properties of graphene, we note that its conductivity can be tuned by changing the chemical potential (or Fermi level), μ_c, by either external electrostatic biasing or chemical doping, at fabrication. This parameter typically ranges from zero, which corresponds to undoped (pristine) and unbiased graphene, up to ± 1 eV (Hanson 2008). The surface conductivity σ_c of graphene contains contributions from intraband and interband transitions triggered by the absorption of photons of energy $\mathscr{E} = \hbar\omega$ and, as such, it can be expressed with the sum $\sigma_c = \sigma_{c,\text{intra}} + \sigma_{c,\text{inter}}$. The intraband contribution term scales almost linearly with μ_c and is given by the Drude-like expression (Falkovsky 2008; Hanson 2008)

$$\sigma_{c,\text{intra}} = i\frac{e^2\mu_c}{\pi\hbar^2(\omega + i/\tau_1)} \times \mathscr{T}\left(\frac{\mu_c}{2k_BT}\right), \tag{9}$$

where $\mathscr{T}(x) = x^{-1}\ln[2\cosh(x)]$, T is the absolute temperature, k_B is the Boltzmann constant and τ_1 is the relaxation time for intraband absorption (Jablan et al 2009). In the optical regime $\tau_1 \approx 10$ fs (Gu et al 2012), while for the THz regime at room temperature $\tau_1 \approx 40$ ps (Otsuji et al 2012). For most practical configurations, the temperature-dependent term can be dropped from Eq. (9), as $\mathscr{T} \to 1$ when $x > 1$, i.e. when $\mu_c > 0.05$ eV for $T = 300$ K. The intraband term is dominant in the THz regime where it contributes to a large imaginary part in σ_c which, it turn, leads to a plasmonic behavior (Bludov et al 2013). The interband term exhibits a pronounced transition when μ_c is tuned near half the photon energy, and is described by the following expression in the optical regime (Falkovsky 2008),

$$\sigma_{c,\text{inter}} = \frac{e^2}{4\hbar}\left\{\frac{1}{2} + \frac{1}{\pi}\tan^{-1}\left[\frac{\hbar\omega_c - 2|\mu_c|}{2k_BT}\right] - \frac{i}{2\pi}\ln\left[\frac{(\hbar\omega_c + 2|\mu_c|)^2}{(\hbar\omega_c - 2|\mu_c|)^2 + (2k_BT)^2}\right]\right\}. \tag{10}$$

where $\omega_c = \omega + i/\tau_2$ is the complex frequency, $\tau_2 \approx 1.2$ ps is the relaxation time for interband absorption (Gu et al 2012), $T \approx 300$ K and $\mu_c > 0.1$ eV. According to Eq. (10), the real part of the interband term becomes negligible, greatly increasing the transparency of the graphene sheet when $\mu_c > 0.5\hbar\omega$; this can be exploited in voltage-controlled absorption modulators (Liu et al 2011). Additionally, the imaginary part of the interband term exhibits a local peaking at $\mu_c \approx 0.5\hbar\omega$ which can be used in phase modulation (Midrio et al 2014; Pitilakis et al 2015). Finally, we note the interband term is typically negligible in the THz regime, except for undoped and unbiased graphene and/or low temperatures.

Moving on to describe the nonlinear properties of graphene, we note that our focus is on its third-order nonlinear surface conductivity tensor, $\bar{\sigma}_s^{(3)}$, in Eq. (3). In the most general

case, $\bar{\bar{\sigma}}_s^{(3)}$ can be described by the hexagonal symmetry group D_{6h} (6/mmm) (Chatzidimitriou et al 2015). If we additionally force that the nonlinear surface current density component normal to the sheet is zero, then this symmetry group allows for up to 14 non-zero elements of which only 6 can be independent. Further simplification can be made if we assume that graphene is a 2D isotropic material, so that $\bar{\bar{\sigma}}_s^{(3)}$ would now have only 8 non-zero elements that all depend on a single complex nonlinear surface conductivity value, σ_3 in $\mathrm{S(m/V)}^2$ units, according to

$$\sigma^{(3)}_{s,jklm} = \sigma_3 \, \frac{1}{3} \left(\delta_{jk}\delta_{lm} + \delta_{jm}\delta_{kl} + \delta_{jl}\delta_{mk} \right). \tag{11}$$

In this expression, δ_{uv} is the Kronecker delta and $\{j,k,l,p\}$ correspond only to the cartesian components that are tangential to the graphene sheet. For instance, when the sheet is normal to the y-axis then $\sigma^{(3)}_{s,xxxx} \equiv \sigma^{(3)}_{s,zzzz} = \sigma_3$ and $\sigma^{(3)}_{s,kkll} \equiv \sigma^{(3)}_{s,klkl} \equiv \sigma^{(3)}_{s,kllk} = \sigma_3/3$, where $\{k,l\} = \{x,z\}$. We stress that the preceding features of $\bar{\bar{\sigma}}_s^{(3)}$ hold when the waveguide coordinate system matches that of the 2D-crystal of graphene. If this is not the case, then $\bar{\bar{\sigma}}_s^{(3)}$ should be rotated from its reference orientation leading to a tensor that can have up to 81 non-zero elements. In the optical frequencies, the scalar nonlinear surface conductivity of graphene can be approximated by (Hendry et al 2010)

$$\sigma_{3,\mathrm{opt}} = -i \, \frac{9 \, e^4 \, v_F^2}{32 \, \omega^4 \, \hbar^3}, \tag{12}$$

where $v_F \approx c_0/300$ is the Fermi velocity in graphene. This expression does not include TPA and has been derived under the conditions $k_B T < |\mu_c| < \hbar\omega$ and the perturbation limits $|\mathbf{E}| \ll \hbar\omega^2/(ev_F)$ and $|\mathbf{E}| \ll |\mu_c|\omega/(ev_F)$ for the electric field. A similar expression for the THz regime can be acquired from Mikhailov and Ziegler (2008),

$$\sigma_{3,\mathrm{THz}} = -i \, \frac{3 \, e^4 v_F^2}{32 \, \omega^3 \hbar^2 \mu_c}. \tag{13}$$

Concluding this subsection, we note that experimental measurements of the optical properties of graphene at the linear regime, especially its absorption related to $\mathrm{Re}\{\sigma_c\}$, converge well with the theoretical formulas presented here (Liu et al 2011; Wu et al 2014). However, that is not the case with the nonlinear optical properties, where experimental measurements diverge considerably depending on the operating wavelength, measurement technique and sample preparation (Cheng et al 2014).

2.3 Finite element implementation

In this section we employ the finite-element method (FEM) (Volakis et al 1998) in order to model graphene-comprising waveguides in the linear regime. As opposed to bulk materials, graphene is introduced as a conductive sheet and is therefore modeled through interface conditions between two bulk media, Eq. (6). Following this approach we avoid modeling graphene sheets as an equivalent ultra-thin bulk medium (Vakil and Engheta 2011). The importance of such a choice is twofold: A Maxwellian macroscopic approach that treats an atom-thick layer as a bulk medium is problematic from a physical perspective and, more importantly, the discretization of regions with sub-nanometer sized geometric features will produce an excessive number of degrees of freedom for the numerical problem. While the

increased computational burden is manageable in a 2D geometries, it can become prohibitive in 3D ones. Finally, we stress that patterned sheet materials exhibiting metal-like properties (e.g. graphene nanoribbon waveguides in the THz band) may produce singular field distribution at their edges, which hinders numerical convergence of linear and especially nonlinear parameters. To avoid such complications in this work, we only consider infinite (or fully wrapped) graphene sheets that have no edges.

In order to apply the Galerkin method we first assume that nonlinearities are absent, i.e. bulk media and graphene sheets are solely described by their linear susceptibility and surface conductivity tensors, respectively. We now take the curl of Eq. (1a) and replace it in Eq. (1b), resulting in the vector wave equation

$$\nabla \times \left(\bar{\mu}_r^{-1} \nabla \times \tilde{\mathbf{E}}\right) - \omega^2 \mu_0 \varepsilon_0 \left(I_3 + \bar{\chi}^{(1)}\right) \tilde{\mathbf{E}} = i\omega\mu_0 \tilde{\mathbf{J}}. \tag{14}$$

Furthermore, we split the current density into its bulk and surface components $\tilde{\mathbf{J}} = \tilde{\mathbf{J}}_b + \tilde{\mathbf{J}}_s \delta_s(\mathbf{r})$ and use Ohm's Law to express them through their respective conductivity tensors, $\bar{\sigma}^{(1)}$ and $\bar{\sigma}_s^{(1)}$, leading to

$$\nabla \times \left(\bar{\mu}_r^{-1} \nabla \times \tilde{\mathbf{E}}\right) - k_0^2 \left(I_3 + \bar{\chi}^{(1)} + i\frac{\bar{\sigma}^{(1)}}{\omega\varepsilon_0}\right) \tilde{\mathbf{E}} = i\omega\mu_0 \bar{\sigma}_s^{(1)} \tilde{\mathbf{E}} \delta_s(\mathbf{r}). \tag{15}$$

We then assume the inner product of vector Eq. (15) with an appropriate test function $\tilde{\mathbf{E}}_\alpha$ and integrate over the entire volume of the problem, V. After some vector algebra, the resulting Galerkin formulation is

$$\iiint_V (\nabla \times \tilde{\mathbf{E}}_\alpha) \cdot [\bar{\mu}_r^{-1} (\nabla \times \tilde{\mathbf{E}})] - k_0^2 \tilde{\mathbf{E}}_\alpha \cdot [\bar{\varepsilon}_\mathrm{r} \tilde{\mathbf{E}}] \, \mathrm{d}V = i\omega\mu_0 \iint_S \tilde{\mathbf{E}}_\alpha \cdot [\bar{\sigma}_s^{(1)} \tilde{\mathbf{E}}] \, \mathrm{d}S, \tag{16}$$

where we used integration by parts, assumed that the E-field vanishes on the external boundary of V and finally substituted $\bar{\varepsilon}_\mathrm{r} = I_3 + \bar{\chi}^{(1)} + i\bar{\sigma}^{(1)}/(\omega\varepsilon_0)$. Examining Eq. (16) we note that its LHS and RHS involve only bulk and sheet medium properties, respectively, and that the triple integration degenerates to a double integration on the graphene surface in the RHS, due to the surface Dirac function. Moreover, assuming the simplest form of the linear surface conductivity tensor, Eq. (8), we can make the following simplification in the RHS of Eq. (16):

$$\iint_S \tilde{\mathbf{E}}_\alpha \cdot [\bar{\sigma}_s^{(1)} \tilde{\mathbf{E}}] \, \mathrm{d}S = \sigma_c \iint_S (\mathbf{n} \times \tilde{\mathbf{E}}_\alpha) \cdot (\mathbf{n} \times \tilde{\mathbf{E}}) \, \mathrm{d}S. \tag{17}$$

Using this expression, all the information of the tensor $\bar{\sigma}_s^{(1)}$ is now contained in σ_c and $\mathbf{n}$, the scalar surface conductivity of graphene and the normal vector, respectively. These can vary within the problem space, describing inhomogeneous and/or arbitrarily oriented sheets. Note that although the RHS of Eq. (17) is derived from a simplified case of the more general conductivity expression, our formalism described by Eq. (16) can handle any form of the $\bar{\sigma}_s^{(1)}$ tensor.

The formulation presented here can be directly used for full 3D-FEM modeling but can also be adjusted straightforwardly for 2D applications. Specifically, when the problem space is 2D, for example a plane, then the volume and surface integrals in Eq. (16) are substituted by surface and line integrals, respectively. In Sections 2.4 and 3 we will investigate nonlinear propagation in longitudinally invariant waveguides thus we are going to utilize the FEM presented here for waveguide eigenmode analysis. To this end, we will adopt the 2D form of Eq. (16) since the problem space is the waveguide cross-section (*xy* plane), thus

casting the electric field as $\tilde{\mathbf{E}} = \mathbf{e}(x,y)\exp(in_{\text{eff}}k_0 z)$, where $\mathbf{e}(x,y)$ is the transverse spectral envelope of a guided mode and n_{eff} is its complex valued effective index, for a specified radiation wavelength. Making this substitution in Eq. (16), we can formulate the waveguide eigenmode problem and extract the effective indices (eigenvalues) and respective transverse field envelopes (eigenvectors) of all supported modes, respectively. The linear eigenmode properties will be used in Section 2.4 to numerically calculate the corresponding nonlinear properties.

2.4 Nonlinear propagation

In this section we derive a set of coupled equations in the NLSE framework (Pitilakis and Kriezis 2013) that describe the propagation in multimode nonlinear waveguides, in the presence of nonlinear bulk and sheet materials. Our ultimate intent is to appraise the nonlinear performance of graphene-comprising waveguides, thus we present here formulae for the calculation of the nonlinear parameters for the waveguide modes, $\gamma_{\text{NL}} = \gamma_{\text{b}} + \gamma_{\text{s}}$, that combine the contribution of both bulk (γ_{b}) and sheet (γ_{s}) nonlinear materials. The nonlinear parameter on its own is not sufficient for the assessment of the overall nonlinear performance of a waveguide design, since the linear and nonlinear losses can severely impair nonlinear operation by limiting the optical power. A more reliable measure is obtained by multiplying γ_{NL} with the propagation length L_{prop}, defined as $L_{\text{prop}} = \lambda/(4\pi\text{Im}\{n_{\text{eff}}\})$ or equivalently as the propagation distance at which the power drops to $1/e$; the larger the L_{prop} the lower the mode attenuation. This figure of merit, $\text{FoM} = \gamma_{\text{NL}} L_{\text{prop}}$, is expressed in units of W^{-1} and is inversely proportional to the threshold power required for the manifestation of Kerr-type nonlinear effects (Pitilakis and Kriezis 2013).

The inclusion of nonlinearity will be effectuated via the customary perturbative fashion, based on the linear solution of Maxwell's wave equations. The overall electric polarization and current density in Eq. (1) are both written as the sum of linear and nonlinear contributions, $\tilde{\mathbf{P}} = \tilde{\mathbf{P}}_{\text{lin}} + \tilde{\mathbf{P}}_{\text{NL}}$ and $\tilde{\mathbf{J}} = \tilde{\mathbf{J}}_{\text{lin}} + \tilde{\mathbf{J}}_{\text{NL}}$, respectively. Please note that the linear terms and the subsequent linear solution have already been discussed in Sections 2.1, 2.2 and 2.3. Substituting the polarization and current density into Eqs. (1) we arrive at the following frequency domain equations,

$$\nabla \times \tilde{\mathbf{E}} = +i\omega\mu_0 \bar{\mu}_{\text{r}} \tilde{\mathbf{H}}, \tag{18a}$$

$$\nabla \times \tilde{\mathbf{H}} = -i\omega \left(\varepsilon_0 \bar{\varepsilon}_{\text{r}} \tilde{\mathbf{E}} + \frac{i}{\omega} \tilde{\mathbf{J}}_{\text{lin}} \right) - i\omega \left(\tilde{\mathbf{P}}_{\text{NL}} + \frac{i}{\omega} \tilde{\mathbf{J}}_{\text{NL}} \right). \tag{18b}$$

Notice how, compared to Eq. (5) of Afshar Vahid and Monro (2009) or Eq. (3) of Daniel and Agrawal (2010), the nonlinear current is added to the nonlinear polarization forming the overall perturbative term $\tilde{\mathbf{P}}'_{\text{NL}}(\omega) = \tilde{\mathbf{P}}_{\text{NL}} + i\omega^{-1}\tilde{\mathbf{J}}_{\text{NL}}$. Thus, the waveguide nonlinear parameter γ_{NL} will be the sum of two distinct contributions that originate from bulk and sheet nonlinear materials that are modeled through nonlinear susceptibility and surface conductivity, respectively.

Following the formalism in Afshar Vahid and Monro (2009), we construct the vector function

$$\tilde{\mathbf{F}} = \tilde{\mathbf{E}}_0 \times \tilde{\mathbf{H}}^* + \tilde{\mathbf{E}}^* \times \tilde{\mathbf{H}}_0, \tag{19}$$

where $\tilde{\mathbf{E}}_0$, $\tilde{\mathbf{H}}_0$ denote the unperturbed fields in the linear regime and $\tilde{\mathbf{E}}$, $\tilde{\mathbf{H}}$ the overall perturbed fields. Equation (19) stems from the Lorentz reciprocity lemma (Snyder and Love

1983) and is also used in the method NEELS (Rapoport 2014); the latter is the development, for the nonlinear case, of the analytical method describing the linear excitations of the waveguide and opened resonators by external sources (Collin 1990). In order to construct a propagation equation set for the multimode waveguide, we will need to consider each forward propagating waveguide mode in turn. To this end, we assume that the unperturbed fields correspond to the p^{th} mode, so that the E-field is expressed as

$$\tilde{\mathbf{E}}_0(\mathbf{r},\omega_0) = \frac{\mathbf{e}^{(p)}(x,y,\omega_0)}{\sqrt{N_p}} e^{i\beta_0^{(p)}z}. \tag{20}$$

Now, the overall perturbed fields are cast as an orthonormal expansion of all forward propagating waveguide modes,

$$\tilde{\mathbf{E}}(\mathbf{r},\omega) = \sum_{q=1}^{M} \tilde{A}_m(z,\omega-\omega_0) \frac{\mathbf{e}^{(q)}(x,y,\omega_0)}{\sqrt{N_q}} e^{i\beta_0^{(q)}z}. \tag{21}$$

In Eqs. (20) and (21): ω_0 is the operating frequency, $\mathbf{e}^{(p)}$ is the transverse envelope profile, $\beta_0^{(p)}$ is the real part of the mode propagation constant at ω_0 (we assume that the losses are low enough to be separately included later) and $\tilde{A}_p$ is the slowly varying (baseband) spectral field envelope that contains both linear dispersion and nonlinear perturbation. The waveguide mode profiles are calculated through linear eigenmode analysis of the waveguide cross-section, applying the theory and numerical techniques described in Sections 2.1, 2.2 and 2.3. The normalization constant N_p is measured in Watts, so that $|\tilde{A}_p|^2$ represents power, and is given by $N_p = 0.5|\iint(\mathbf{e}^{(p)} \times \mathbf{h}^{(p)*}) \cdot \mathbf{z}\mathrm{d}S|$; the integral is calculated over the waveguide cross-section while the integrand corresponds to the time-averaged guided power density, derived from the Poynting vector. The normalization constant N_p can be related to the mode orthogonality (Snyder and Love 1983) that holds for lossless and low loss waveguides alike.

Having associated the perturbed and unperturbed fields through $\tilde{\mathbf{F}}$, we now apply the conjugated reciprocal theorem over the waveguide cross-sectional plane,

$$\iint \nabla \cdot \tilde{\mathbf{F}} \, \mathrm{d}S = \frac{\partial}{\partial z} \iint \tilde{\mathbf{F}} \cdot \hat{\mathbf{z}} \, \mathrm{d}S. \tag{22}$$

To construct the final set of propagation equations in the time-domain, we combine Eqs. (18) through (22) using the vector identity $\nabla \cdot (\tilde{\mathbf{E}}_0 \times \tilde{\mathbf{H}}^*) = \tilde{\mathbf{H}}^* \cdot (\nabla \times \tilde{\mathbf{E}}_0) - \tilde{\mathbf{E}}_0 \cdot (\nabla \times \tilde{\mathbf{H}}^*)$, we assume that the nonlinear terms have instantaneous response around ω_0 and we apply the inverse Fourier transform, finally arriving at

$$\frac{\partial A_p}{\partial z} = \sum_{n=1}^{\infty} \frac{i^{n+1}}{n!} \beta_n^{(p)} \frac{\partial^n}{\partial t^n} A_p + \frac{i\omega_0 e^{i\omega_0 t}}{2\sqrt{4N_p}} e^{-i\beta_0^{(p)}z} \times \\ \times \left[\left(1 + \frac{i}{\omega_0}\frac{\partial}{\partial t}\right) \iint \mathbf{e}^{(p)*} \cdot \mathbf{P}_{\text{NL}} \mathrm{d}S + \frac{i}{\omega_0} \iint \mathbf{e}^{(p)*} \cdot \mathbf{J}_{\text{NL}} \mathrm{d}S \right], \tag{23}$$

where $\beta_n^{(p)}$ is the n^{th} derivative of the p^{th} mode propagation constant with respect to ω evaluated at ω_0. Note that the $\partial/\partial t$ only appears in the polarization term, since in Eq. (1) the current density $\tilde{\mathbf{J}}$ has no time derivative, so we can infer that nonlinear current densities have no contribution to self-steepening phenomena (Agrawal 2007). In this work we focus on graphene which is modeled through a nonlinear sheet current, so we will entirely

drop the time-derivative term from Eq. (23). Finally, note that Eq. (23) does not include linear attenuation terms, which will be added heuristically in what follows, assuming that the propagation length is typically much larger than the radiation wavelength.

The NLSE set described by Eq. (23) is general in the sense that it holds for any instantaneous nonlinear process originating in bulk and sheet media; a similar formulation can be derived within the framework of the NEELS method Rapoport (2014). Specializing Eq. (23) for electromagnetic propagation in graphene-comprising waveguides, we need to define the form of nonlinear surface current density on graphene. Even order processes in Eq. (3) identically vanish owing to the unit cell symmetry of graphene, thus leaving the third order nonlinearity as the dominant contribution. Thus, we can express the nonlinear surface current density as $\mathbf{J}_{\mathrm{NL}} = \delta_{\mathrm{s}}(\mathbf{r})\mathbf{J}_{\mathrm{s,NL}} = \delta_{\mathrm{s}}(\mathbf{r})\bar{\sigma}_s^{(3)}|\mathbf{EEE}$ where the vertical bar denotes tensorial multiplication. For narrowband third order nonlinear effects (Kerr/TPA and FWM), the j^{th} cartesian component of the nonlinear surface current density is

$$J_{s,j,\mathrm{NL}} = \mathbf{J}_{\mathrm{s,NL}} \cdot \mathbf{j} = \frac{3}{4}\sum_{klm}^{xyz} \sigma^{(3)}_{s,jklm} E_k E_l^* E_m, \tag{24}$$

where the subscripts $\{j,k,l,m\}$ denote cartesian components, i.e. $\{x,y,z\}$, and $\sigma^{(3)}_{s,jklm}$ are the 81 complex-valued elements of the fourth-rank tensor $\bar{\sigma}_s^{(3)}$ discussed in Section 2.2. Similarly, the nonlinear polarization is expressed through the third-order nonlinear susceptibility for bulk materials as (Boyd 2008)

$$P_{j,\mathrm{NL}} = \mathbf{P}_{\mathrm{NL}} \cdot \mathbf{j} = \frac{3}{4}\sum_{klm}^{xyz} \chi^{(3)}_{jklm} E_k E_l^* E_m. \tag{25}$$

Having defined $\mathbf{J}_{\mathrm{NL}}$ for graphene, we combine Eqs. (20)-(21) and (23)-(25) to extract a set of coupled NLSE that describe the simultaneous propagation of M modes in a graphene comprising waveguide

$$\frac{\partial A_p}{\partial z} = -\frac{\alpha_p}{2}A_p + \sum_{n=1}^{\infty}\frac{i^{n+1}}{n!}\beta_n^{(p)}\frac{\partial^n}{\partial t^n}A_p + i\sum_{abc=1}^{M}\gamma_{pabc}e^{i\Delta\beta_{pabc}z}A_a A_b^* A_c, \tag{26}$$

where $\gamma_{pabc} = \gamma_{pabc}^{(\mathrm{bulk})} + \gamma_{pabc}^{(\mathrm{sheet})}$ is the total nonlinear parameter and the indices $\{p,a,b,c\}$ denote the modes of the waveguide. γ_{pabc} can correspond to nonlinear processes like FWM, self-phase or cross-phase modulation, depending on the indices $\{p,a,b,c\}$, (Pitilakis and Kriezis 2013). Bulk and sheet contributions, in their most general form, are given by

$$\gamma_{pabc}^{(\mathrm{bulk})} = \frac{3\omega_0\varepsilon_0}{16\sqrt{N_p N_a N_b N_c}}\sum_{jklm}^{xyz}\iint \chi^{(3)}_{jklm} e_j^{(p)*} e_k^{(a)} e_l^{(b)*} e_m^{(c)}\,\mathrm{d}S, \tag{27a}$$

$$\gamma_{pabc}^{(\mathrm{sheet})} = \frac{3i}{16\sqrt{N_p N_a N_b N_c}}\sum_{jklm}^{xyz}\int \sigma^{(3)}_{s,jklm} e_j^{(p)*} e_k^{(a)} e_l^{(b)*} e_m^{(c)}\,\mathrm{d}\ell, \tag{27b}$$

where $\Delta\beta_{pabc} = -\beta_0^{(p)} + \beta_0^{(a)} - \beta_0^{(b)} + \beta_0^{(c)}$ represents phase mismatch and is real valued owing to how β_0 was defined. Equation (26) also includes linear losses introduced heuristically, where α_p is the linear power absorption coefficient of the mode defined as $\alpha_p = 4\pi\mathrm{Im}\{n_{\mathrm{eff}}\}/\lambda = 1/L_{\mathrm{prop}}$. Note how the double integration on the bulk surface current $\mathbf{J}_{\mathrm{NL}}$ in Eq. (23) was converted into a line integration along the trace of graphene sheet on the waveguide cross section, through the surface Dirac function. Furthermore, we can

observe that Eq. (26) contains distinct terms associated with bulk and sheet nonlinear materials, which will eventually lead to distinct complex-valued nonlinear parameters, Eqs. (27). While the real part of $\chi^{(3)}_{jklm}$ is responsible for the nonlinear phase-shift in bulk materials, it is the imaginary part of $\sigma^{(3)}_{s,jklm}$ that produces the same response in sheet materials. Similarly, the introduction of TPA from graphene could be readily realized through the real part of its nonlinear conductivity. However, due to lack of sufficient experimental and theoretical data, TPA will be excluded from the calculations in this work.

Finally, we present the simplest version of Eq. (26) corresponding to a singlemode waveguide,

$$\frac{\partial A}{\partial z} = -\frac{\alpha}{2}A + \sum_{n=1}^{\infty} \frac{i^{n+1}}{n!}\beta_n \frac{\partial^n}{\partial t^n}A + i(\gamma_b + \gamma_s)|A|^2 A, \tag{28}$$

using also the simplest versions of the sheet (γ_s) and bulk (γ_b) nonlinear parameters of Eqs. (27),

$$\gamma_b = \frac{\omega_0 \varepsilon_0}{(2N)^2} \iint \chi_3 \left(\frac{1}{2}|\mathbf{e}|^4 + \frac{1}{4}|\mathbf{e}\cdot\mathbf{e}|^2 \right) \mathrm{d}S, \tag{29a}$$

$$\gamma_s = i\frac{1}{(2N)^2} \int \sigma_3 \left(\frac{1}{2}|\mathbf{e}_\parallel|^4 + \frac{1}{4}|\mathbf{e}_\parallel \cdot \mathbf{e}_\parallel|^2 \right) \mathrm{d}\ell. \tag{29b}$$

In Eq. (29a), bulk material nonlinearity is assumed isotropic and is expressed through the complex scalar value $\chi_3 = (4/3)c_0\varepsilon_0 n_0^2 n_2$, where n_2 (m^2/W) is the complex-valued nonlinear index, whose real and imaginary parts quantify the Kerr-effect and TPA magnitude, respectively (Daniel and Agrawal 2010). In Eq. (29b), we have adopted the simplest form of the nonlinear surface conductivity tensor $\bar{\bar{\sigma}}^{(3)}_s$, Eq. (11), depending on a single σ_3 value.

3 Linear and nonlinear waveguide calculations

In this section we will study representative examples from three families of optical waveguides: High index-contrast integrated waveguides represented by silicon wire and slot configurations, Fig. 1(a)-(b); plasmonic waveguides in stripe and slot configurations, Fig. 1(c)-(d); low index-contrast waveguides such as glass microfibers, Fig. 1(e). Graphene sheets will be added to these waveguides and several arrangements will be discussed in order to identify optimal designs and parameter choices for nonlinear applications.

Our focus is in the near infrared (NIR) spectral region, $\lambda = 1550$ nm, where graphene sheets only negligibly affect waveguiding, owing to the relatively small $\mathrm{Im}\{\sigma_c\}$. This perturbative behavior of graphene in the NIR region is in stark contrast to the THz region, where its metal-like properties are so pronounced that it can guide SPP waves along its own surface (Bludov et al 2013). In all the simulations performed in this section, unless otherwise stated, we assume homogeneous, flat and unpatterned graphene monolayers at room temperature ($T = 300$ K) and at a chemical potential of $\mu_c = 0.5$ eV; please note that for $\mu_c > 0.4$ eV the interband absorption mechanism at $\lambda = 1550$ nm is negligible, significantly reducing waveguide losses. In this case, using the formulas and parameters presented in Section 2.2, Eqs. (9), (10) and (12), the linear and nonlinear surface conductivity of graphene monolayers are $\sigma_c = 8.92 + i5.78\ \mu\mathrm{S}$ and $\sigma_3 = -i7.21 \times 10^{-23}\ \mathrm{S(m/V)^2}$, respectively.

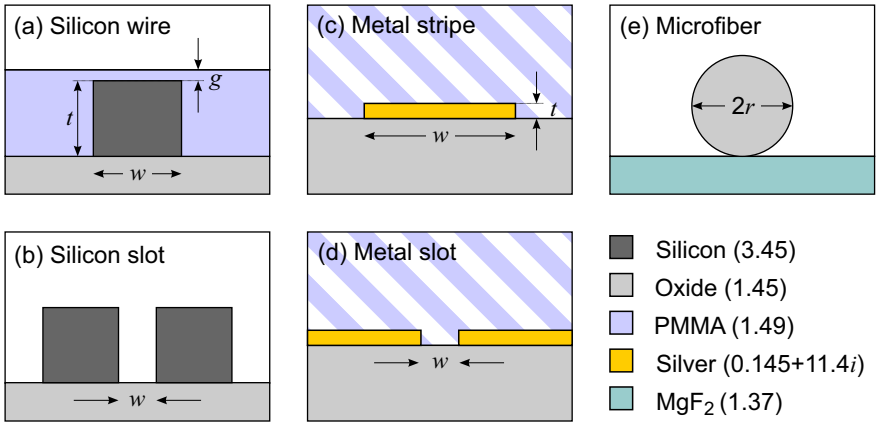

Fig. 1 (a)-(b) Silicon wire and slot configurations, (c)-(d) metal stripe and slot plasmonic waveguides clad with either air or PMMA, (e) glass microfiber. Critical dimensions for each waveguide are annotated on the figures and material color-key along with their refractive indices are given in the bottom right panel. Graphene sheets are not displayed in this figure.

3.1 Silicon waveguides

Silicon on insulator (SOI) is the de facto platform for integrated photonics, mature from the fabrication standpoint and compatible with CMOS microelectronic technology. The strong index contrast between silicon and oxide/air can be exploited in fabricating subwavelength waveguides that provide increased mode confinement which, combined with high nonlinear index of silicon, $n_2 = 2.5 \times 10^{-18}$ m^2/W (Daniel and Agrawal 2010), leads to considerable nonlinear performance.

For our first example, we assume a 340 nm-thick silicon wire ($n = 3.45$) over an oxide substrate ($n = 1.45$). The waveguide is covered with PMMA ($n = 1.49$) forming a flat surface at a distance $g = 20$ nm from the top of the underlying silicon wire, Fig. 1(a), where an infinite graphene monolayer is located. We numerically extract the TE and TM eigenmodes supported by this graphene-comprising waveguide and calculate: their nonlinear parameters attributed to bulk-silicon (γ_b) and graphene-sheet (γ_s) contributions, Fig. 2(a); their graphene-conductivity induced propagation losses, Fig. 2(b); their nonlinear FoM, Fig. 2(c). Firstly, we note that the trend of the red curves for γ_s and losses is the same, i.e., increased nonlinearity is always accompanied by increased losses for graphene. Peaks in these curves designate waveguide designs where the mode interacts strongly with graphene, as a result of the increased confinement of the E-field tangential to the sheet. Furthermore, the nonlinear figure-of-merit stemming from graphene nonlinearity and losses, FoM $= \gamma_s L_{\text{prop}}$, is more strongly affected by γ_s, as depicted by the red curves of Fig. 2(c) that rise as the Si-width decreases. In comparison to regular Si-wire waveguides without graphene, we notice that the graphene-sheet nonlinear parameter is about ten times smaller than the bulk-silicon one. Moreover, state of the art Si-wire losses stemming mostly from fabrication imperfections are in the order of 0.1 dB/mm (1 dB/cm), i.e. one to two orders of magnitude smaller compared to graphene losses, Fig. 2(b). This two-fold superiority of regular Si-wire waveguides without graphene is reflected on the FoM which, for their case, is typically larger than 1 W^{-1} (Pitilakis and Kriezis 2013) but is considerably decreased when graphene is added, Fig. 2(c).

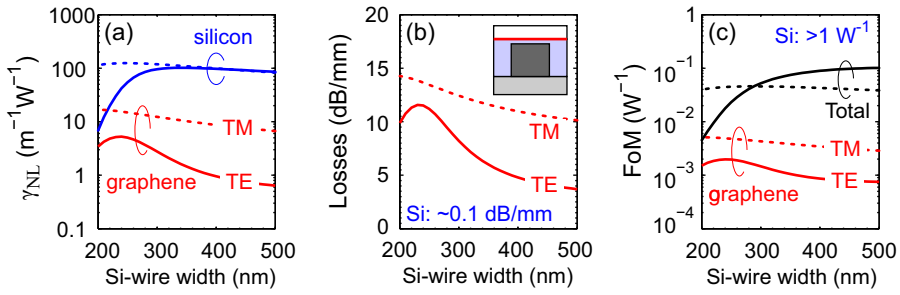

Fig. 2 (a) Nonlinear parameters attributed to bulk-silicon and graphene-sheet contributions; TE and TM modes are depicted with solid and dotted curves, respectively. (b) Propagation losses owing to graphene conductivity; inset depicts the placement of the graphene sheet with the red horizontal line; current state of the art for Si-wire losses is approximately 0.1 dB/mm. (c) Overall figure-of-merit, $\gamma_{NL}L_{prop}$, taking into account either the total nonlinear parameter, black curves, or just the graphene nonlinear parameter, red curves.

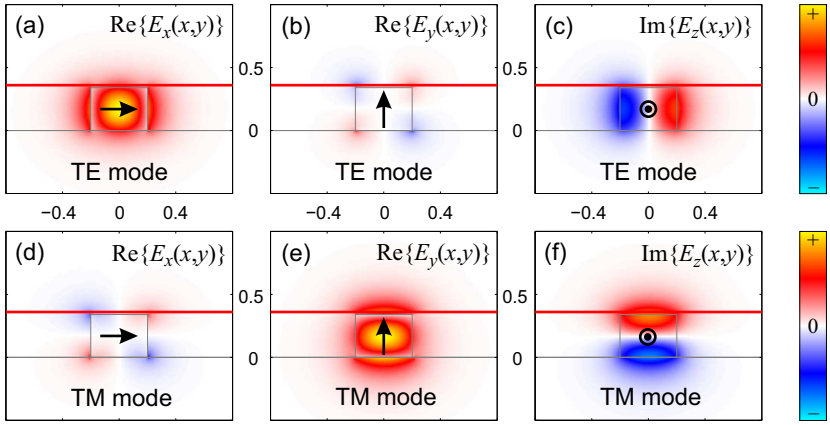

Fig. 3 Electric field distribution in the waveguide cross-section, *xy*-plane. Si-wire is 400 nm wide and 340 nm thick, covered with PMMA and a graphene sheet (thick horizontal red line), leaving a 20 nm-thick PMMA gap between wire and graphene. (a)-(c) *x*-, *y*- and *z*-components of the TE mode; (d)-(f) *x*-, *y*- and *z*-components of the TM mode.

Commenting on the polarization dependence exhibited by this waveguide, Fig. 2, one would intuitively expect the TE mode to have stronger interaction with graphene compared to the TM mode, owing to its stronger *x*-component, Fig. 3(a) *vs.* 3(d), and thus have higher losses and nonlinearity. However, that is not the case and this can be attributed to the longitudinal *z*-component of the E-field, which is stronger on the graphene sheet for the TM mode, Fig. 3(f). Consequently, in order to maximize the interaction of TE-polarized modes with graphene, the horizontal sheet should be displaced towards the center of the Si-wire where E_x is most intense. As for maximizing the interaction of TM-polarized modes with graphene, placing the sheet exactly on the top face of the Si-wire is actually the optimal choice.

Seeking to optimize silicon-based graphene-comprising waveguides, we presently turn to the slot design, Fig. 1(b) (Koos et al 2007). The E-field in this waveguide is TE-polarized and strongly confined inside the narrow low-index slot formed between two high-index silicon ridges. Mode confinement increases for slot materials with lower refractive indices so we dismiss PMMA for this design and assume an air-filled slot design where a flat graphene

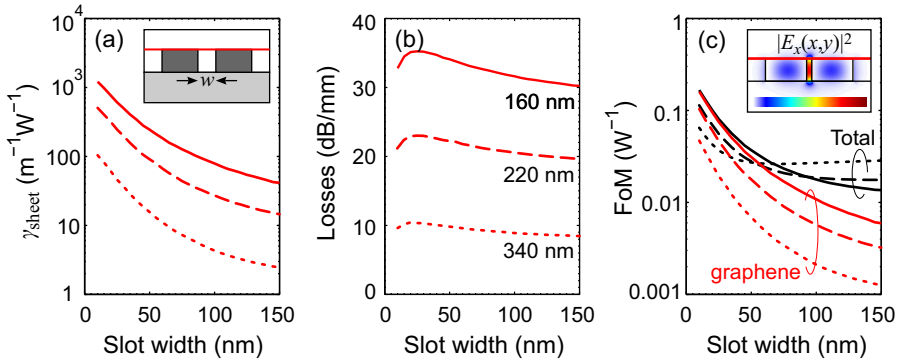

Fig. 4 Parametric investigation of the TE mode supported by the slot waveguide formed by two 400 nm-wide Si-wires as a function of the slot width, for three Si-wire thicknesses. (a) Nonlinear parameter of graphene sheet, (b) propagation losses, (c) overall FoM assuming: the total nonlinear parameter, black curves, or only graphene nonlinear parameter, red curves.

sheet is placed horizontally on top of the two 400 nm-wide Si-wires, as depicted in the inset of Fig. 4(a). The intensity distribution of the dominant transverse component of the TE-polarized mode supported by this waveguide, $|E_x(x,y)|^2$, is depicted in the inset of Fig. 4(c). We numerically extract its linear and nonlinear properties as a function of the slot width, for the fabrication standard Si-wire thicknesses of 340, 220 and 160 nm. Evidently, the graphene nonlinear parameter increases as the slot width and wire thickness decrease, Fig. 4(a), whereas the bulk nonlinear parameter originating from silicon (not shown) remains approximately constant at $\gamma_b \approx$ 40-65 $\mathrm{m^{-1}W^{-1}}$ for all configurations. The overall FoM, dominated by graphene nonlinearity for slot widths below 50 nm, reaches up to $\mathrm{FoM} = 0.1\ \mathrm{W^{-1}}$ thus offering a slight improvement compared to the graphene-comprising Si-wire waveguide previously discussed. As with the Si-wire, we note that the FoM has a greater dependance on γ_s compared to graphene losses. Finally, further tuning the geometric parameters of the slot design, for example decreasing the Si-wire width or considering even narrower slots, might provide a small improvement to nonlinear performance in terms of the FoM, but it detracts from practical implementations.

3.2 Plasmonic waveguides

Plasmonic waveguides can be formed at the interfaces between dielectrics and materials characterized by a relative dielectric permittivity (ε_r) with a negative real part of large absolute value; the E-field of the so called SPP waves is polarized perpendicularly to these interfaces and is strongly confined to it. In the NIR spectral region, metals are known to exhibit this behavior, i.e., $\mathrm{Re}\{\varepsilon_r\} \ll -1$, but their ε_r also contains a non-negligible imaginary part related to absorption. Consequently, SPP waves suffer considerable propagation losses even though they penetrate little into the metal. Interestingly, graphene exhibits such metal-like properties in the THz region and is thus capable to support plasmonic modes, as has been theoretically proposed, for example with air-suspended nanoribbon waveguides (Nikitin et al 2011). For the 1550 nm band, silver (Ag) with $\varepsilon_r = -130 + 3.3i$ is an excellent candidate for SPP waveguides as it leads to lower losses compared to gold or copper.

In this Section, we will consider the two main archetypes of plasmonic 3D waveguides: the stripe and slot configurations, Fig. 1(c) and 1(d), respectively. The former consists of a

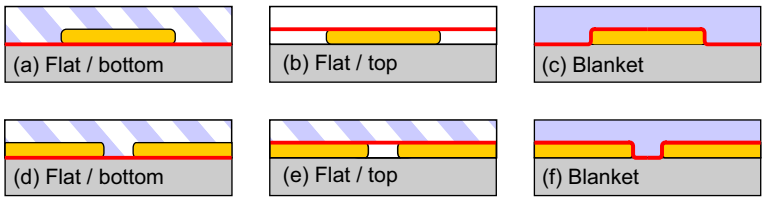

Fig. 5 Possible placement of graphene sheet (thick red lines) with respect to metal film for (a)-(c) stripe and (d)-(f) slot plasmonic waveguides. Air and PMMA cladding is considered for configurations (a), (d) and (e). The color-key for the bulk materials is the same as in Fig. 1.

20 nm-thick and 1 μm-wide silver stripe on top of an oxide substrate and clad with either air or PMMA; the latter consists of a 50 nm-wide slot on a 20 nm-thick silver stripe, also clad with either air or PMMA. The symmetry of substrate and cladding bulk dielectrics affects the plasmonic mode losses and confinement; that is why PMMA was chosen as a cladding material, having a refractive index close to that of the silicon dioxide substrate. Graphene will be added to these plasmonic waveguides and we will numerically calculate their linear and nonlinear properties. In this way, we will identify the optimal placement of the graphene sheet, namely under or over the metal film layer as in Fig. 5, that maximizes its interaction with the plasmonic mode. In both stripe and slot configurations, when the graphene is placed over the metal and the structure is coated with PMMA, the graphene sheet can be pressed down thus assuming the relief underneath it, i.e., it "blankets" the metal, as in Fig. 5(c) and 5(f), or, detailed, in Fig. 6. Nevertheless, we will also consider the slot configuration where the graphene sheet covering a narrow slot remains flat despite the pressure of the PMMA cladding as in Fig. 5(e).

At this point, we stress that when modeling plasmonic waveguides with the FEM, acute geometric features on the metal/dielectric interfaces, e.g. the right angles at the corners of the metal layers, Fig. 6(a), lead to singularities manifesting as increased mode confinement there; the singularities are more pronounced as the angle becomes more acute (Pitilakis and Kriezis 2013). Consequently, as graphene sheets are placed near (or on) those features, we noticed that the line integral for the calculation of γ_s from the tangential field components, for example through Eq. (29b), does not numerically converge. Moreover, this fact also reveals that γ_s is dominated by the E-field that is highly-localized on these acute features. To address these issues, as well as to realistically model fabricated structures, all right angles of the metal layers are rounded assuming quarter-circle segments ("fillets") of $r_c = 2$ nm curvature radius, Fig. 6(b). Closing this remark, we point out that the aforementioned features do not significantly affect the convergence of the linear mode properties in these waveguides, namely the effective index n_{eff} or the propagation length; only the parameters that depend on mode confinement close to the singularities are affected. A similar problem is expected when modeling patterned graphene sheets in the THz band, for example graphene nanoribbon waveguides which resemble plasmonic metal stripe waveguides: the singular mode distribution at the two edges of the nanoribbon leads to extremely high calculated nonlinear parameter (Chatzidimitriou et al 2015) that moreover converges slowly. The previously described fillet technique can not be applied to these sheet media, so modeling them using ultra-thin bulk medium layers (with fillets) is the surest way to achieve converged results at the expense of computational burden. In any case, we do not deal with graphene sheets in the THz band in the present work.

Before we look into the nonlinear parameter calculation for the stripe and slot plasmonic optical waveguides, we will assess their linear attenuation which also plays an important role

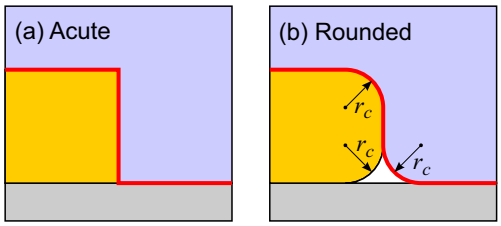

Fig. 6 Detail of graphene-blanketed metal stripe with (a) acute or (b) rounded corners, also called fillets. The structure is clad with PMMA that presses down the graphene sheet (thick red line) and forms an air pocket in (b). We used curvature radius $r_c = 2$ nm in all the simulations performed in this section.

in nonlinear optics. Propagation losses in these high confinement waveguides were found to be dominated by the bulk conductivity of the metal (silver). When all graphene sheets are removed, the propagation lengths of the air-clad stripe and slot waveguides are 45 and 13 μm, respectively; for the PMMA-clad configurations, the propagation lengths are decreased to 20 and 10 μm for stripe and slot configurations, respectively. Therefore, in the simulations that follow, we have switched-off the silver conductivity, assuming $\varepsilon_r = -130$ or, equivalently, $n = i11.4$. In this way, the propagation length extracted by our eigenmode solver is only due to graphene surface conductivity, $\mathrm{Re}\{\sigma_c\}$. In all cases, we verified that the overall propagation length can be approximated fairly well by $L_{\mathrm{prop},T}^{-1} = L_{\mathrm{prop},b}^{-1} + L_{\mathrm{prop},s}^{-1}$, where the propagation length due to sheet (or bulk) conductivity, $L_{\mathrm{prop},s}$ (or $L_{\mathrm{prop},b}$), is calculated from the eigenmode solver with the bulk (or sheet) conductivity switched off. This approximation stands as long as graphene negligibly perturbs the mode profile, which was always the case for the infrared wavelength band and for the graphene parameters employed.

We start with the stripe plasmonic waveguide which, dominated by metal/dielectric interfaces normal to the *y*-axis, supports TM-polarized modes. For nonlinear applications, we will utilize the *y*-antisymmetric TM mode, Fig. 7(a)-(c), characterized by high confinement and increased losses. In fact, this mode can be deconstructed as the superposition of the edge SPP modes supported by two semi-infinite metal stripes, merged to form a finite-width stripe. On a side note, the low-loss (or "long-range") *y*-symmetric TM mode commonly employed in integrated plasmonic components is far less confined and additionally requires wider metal stripes; the symmetric mode is inferior to the antisymmetric one in terms of the overall nonlinear FoM and, as explained, it considerably increases the waveguide dimensions, thus forfeiting the subwavelength plasmonic trait. Returning to the antisymmetric TM mode, we note that its confinement (especially localized on the four rounded corners of the metal layer) increases as the metal stripe thickness and width decreases; the 20 nm thickness and 1 μm width were chosen as realistic lower limits in state of the art fabrication techniques. Proceeding to the presentation of our results for the plasmonic stripe configurations, Fig. 5(a)-(c), the first four rows of Table 1 contain the nonlinear parameter ($\gamma_{\mathrm{NL}} = \gamma_s$), the sheet and total propagation lengths ($L_{\mathrm{prop},s}$ and $L_{\mathrm{prop},T}$) and the overall FoM $= \gamma_{\mathrm{NL}} L_{\mathrm{prop},T}$. As pointed out, the propagation length due to graphene-sheet conductivity is much higher than the one for bulk-silver conductivity, meaning that the latter will eventually dominate. In this sense, one should only seek to maximize the γ_{NL}, which is higher when graphene is placed on the side of the metal in contact with the higher-index dielectric. The best performing configuration is the one where graphene blankets the metal stripe, but the overall FoM is less than 0.01 W^{-1} when both bulk and sheet conductivity losses are accounted for.

Subsequently, we assess the performance of the plasmonic slot configuration, formed by a 50 nm-wide slot on a 20 nm-thick silver film. This waveguide supports a TE-mode (*x*-polarized), highly confined inside the slot, Fig. 7(d)-(f). Similarly to the stripe configuration, this mode can be considered as a superposition of two edge SPP modes supported by semi-infinite metal stripes, and its confinement increases as the slot width and metal thick-

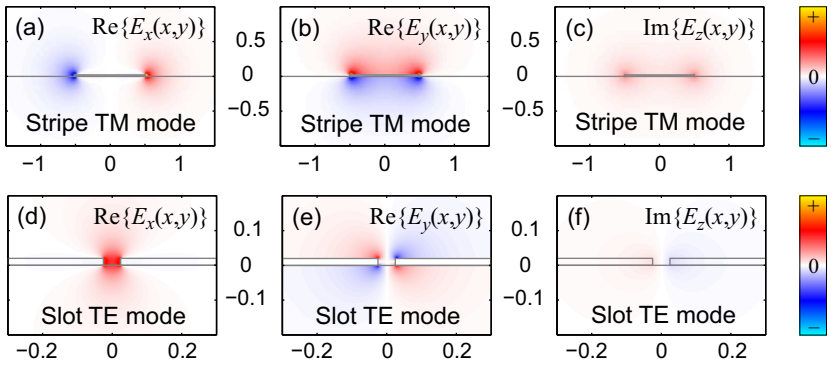

Fig. 7 Electric field distribution of the metal-stripe and -slot plasmonic waveguide modes. Both structures are PMMA-clad and without any graphene sheets. (a)-(c) *x*-, *y*- and *z*-components for the anti-symmetric TM mode of the metal stripe; (d)-(f) *x*-, *y*- and *z*-components for the TE mode of the metal slot.

Table 1 Nonlinear performance of graphene-comprising plasmonic waveguides, namely the 1 μm-wide stripe and 50 nm-wide slot configurations. In all cases, the substrate is silicon oxide and the metal is 20 nm-thick silver, with all its corners rounded with a 2 nm curvature radius.

Type	Graphene [Fig.]	Cladding	γ_{NL} ($m^{-1}W^{-1}$)	$L_{p,s}$ (μm)	$L_{p,T}$ (μm)	FoM (W^{-1})
Stripe	Flat/Bottom [5(a)]	Air	2.12×10^{2}	212	37	0.0079
Stripe	Flat/Bottom [5(a)]	PMMA	3.68×10^{2}	118	17	0.0063
Stripe	Flat/Top [5(b)]	Air	0.84×10^{2}	264	38	0.0032
Stripe	Blanket/Top [5(c)]	PMMA	5.65×10^{2}	111	17	0.0096
Slot	Flat/Bottom [5(d)]	Air	2.66×10^{4}	19.7	7.8	0.2083
Slot	Flat/Bottom [5(d)]	PMMA	1.90×10^{4}	25.5	7.2	0.1365
Slot	Flat/Top [5(e)]	Air	1.97×10^{4}	20.7	8.0	0.1573
Slot	Flat/Top [5(e)]	PMMA	2.38×10^{4}	24.0	7.1	0.1680
Slot	Blanket/Top [5(f)]	PMMA	2.68×10^{4}	23.8	7.0	0.1887

ness decreases. The last five rows of Table 1 contain the nonlinear parameter, propagation lengths (sheet and total) and overall FoM, for the plasmonic slot configurations presented in Fig. 5(d)-(f). We note that the γ_{NL} is considerably increased compared to the stripe configurations, whereas the total propagation length is only fractionally diminished; the net effect is a FoM twenty times higher, up to 0.2 W^{-1}. Finally, it can be inferred that, for the plasmonic slot waveguide, the graphene placement, top or bottom, and the cladding material only marginally affect the nonlinear performance.

3.3 Microfiber waveguides

In this last subsection, we will focus on low index-contrast dielectric waveguides and specifically on a glass microfiber residing on a magnesium fluoride (MgF_2) substrate, Fig. 1(e).

As with all the previously studied optical waveguides, graphene acts as a perturbation to the microfiber waveguide, having a negligible impact on Re$\{n_{eff}\}$. However, its effect on propagation losses and sheet nonlinearity is important, especially when graphene interacts strongly with the E-field of the mode. This takes place when the fundamental microfiber mode is weakly guided, for example for small radii; in this case, the mode is not highly

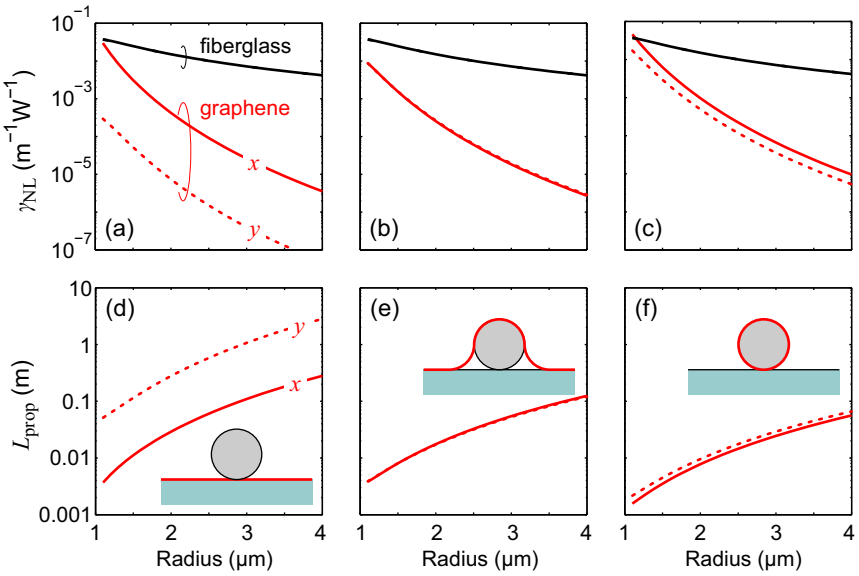

Fig. 8 Bulk and sheet nonlinear parameters for *x*- and *y*-polarized modes of the microfiber-on-MgF2 waveguide when graphene is placed (a) under, (b) covers, (c) is wrapped around the microfiber. (d)-(e) Graphene-induced propagations losses for the previously mentioned arrangements, respectively.

confined inside the glass core and is thus allowed to overlap with graphene. On the other hand, the microfiber radius should be $r > 1.1$ μm at $\lambda = 1550$ nm to avoid leaking into the MgF_2 substrate, i.e. to ascertain that $\mathrm{Re}\{n_{\mathrm{eff}}\} > 1.37$ for both polarizations. In the simulations performed in this section we assumed a bulk nonlinearity of $n_2 = 2.7 \times 10^{-20}$ m^2/W for the fiberglass and zero for the MgF_2 substrate.

Figure 8 presents the γ_{NL} and L_{prop} for the *x*- and *y*-polarized modes of the microfiber as a function of its radius, for three arrangements of the graphene sheet depicted in the insets with thick red lines. The simplest setup, where a graphene sheet covers the MgF_2 substrate before the microfiber is positioned, is presented in Figs. 8(a) and (d). We note: firstly, that the bulk fiberglass nonlinearity is almost identical for the *x*- and *y*-polarized modes (dotted and solid black curves cannot be distinguished in the figure) and is larger than graphene sheet nonlinearity; secondly, that there is a difference between the two polarizations, with the *x*-polarized mode interacting more strongly with graphene; thirdly, that γ_s decreases (and L_{prop} increases) considerably as the microfiber radius increases. State of the art attenuation in glass microfibers is in the order of 1 dB/m (Leon-Saval et al 2004) and so the aggregate waveguide losses are dominated by graphene conductivity. This, along with the fact that fiberglass bulk nonlinearity dominates over sheet nonlinearity, is reflected on the overall FoM (not shown) which is higher for the low-loss *y*-polarized mode and increases as the radius increases, but barely exceeds 0.01 W^{-1} for $r > 3.5$ μm.

This graphene-comprising microfiber waveguide configuration was recently used in a FWM experiment (Wu et al 2014) providing evidence of strong nonlinear response from graphene: When the MgF_2 substrate was covered by a graphene sheet before depositing a $r = 1.1$ μm microfiber, i.e., as in the inset of Fig. 8(d), then the FWM-generated power at the idler wavelength was increased by as much as 30 dB compared to the case of the microfiber residing on a bare MgF_2 substrate, Fig. 1(e). Assuming the optical power levels ($P \approx$

100 mW), the measured graphene-induced losses (1 dB/mm) and the resulting conversion efficiency ($\eta \approx -30$ dB) of the experiment, we estimate an overall $\gamma_{\rm NL} > 100$ m^{-1}W^{-1} for the waveguide used in that experiment, based on the approximate formula FoM $= \gamma_{\rm NL} L_{\rm prop} \approx 3\sqrt{\eta}/P$ (Pitilakis and Kriezis 2013; Agrawal 2007). Subsequently, we calculated the nonlinear parameters for the *x*-polarized mode of the graphene-comprising microfiber waveguide using our formulation, yielding $\gamma_b = 0.037$ m^{-1}W^{-1} and $\gamma_s = 0.03$ m^{-1}W^{-1}, Fig. 8(a). Comparing these values to the experimentally extracted one, we can deduce that the nonlinear surface conductivity of graphene (σ_3) can be up to three orders of magnitude larger than the one predicted by the formula of Hendry et al (2010) and used in this work. Needless to say that such a difference would have a tremendous impact on the performance of the previously analyzed integrated subwavelength waveguides.

We have also investigated the design where the graphene sheet is placed on top of the microfiber, Figs. 8(b) and (e), covering half of its circumference. Interestingly, this configuration leads to approximately the same γ_s (and $L_{\rm prop}$) for the *x*- and *y*-polarized modes since the part of graphene that interacts with the field is situated far from the MgF_2 substrate which is responsible for breaking the degeneracy of the two microfiber modes. Finally, Figs. 8(c) and (f) contain the $\gamma_{\rm NL}$ and $L_{\rm prop}$, respectively, for the fictitious case where a graphene monolayer is fully wrapped around the microfiber. We note that the difference between the *x*- and *y*-polarized modes is somewhat more pronounced than the previous case, but not as pronounced as in the first setup.

4 Summary and conclusions

In this paper we have presented a rigorous formalism for the extraction of linear and nonlinear parameters in graphene-comprising waveguides. We started our analysis from the linear problem, where we presented how graphene can be implemented through Maxwell's equations as a conductive sheet/2D medium or, in other words, as an interface condition in the FEM which we used in our numerical simulations. We discussed how the sheet representation of graphene is superior to the equivalent bulk/3D medium representation, both in terms of underlying physical consistency and computational efficiency. In the nonlinear regime, a NLSE formalism was developed for the extraction of the nonlinear parameters of graphene-comprising waveguides. The set of coupled equations presented describe the nonlinear pulse propagation of an arbitrary number of distinct modes/signals in these waveguides. The nonlinearity of graphene was fully modeled through its nonlinear surface conductivity tensor, extracted from existing theoretical modes, and introduced via a perturbation method. We showed how the overall nonlinear parameter can be split into distinct parts representing bulk and sheet medium contributions. Note that although we focused our attention on third-order narrowband phenomena (namely Kerr/TPA effects and FWM), our analysis has a general scope and can be specialized to describe other nonlinear phenomena, as long as they satisfy the approximations made, i.e., having an instantaneous response and being small perturbations compared to the linear response. Finally, we studied three representative graphene-comprising waveguide configurations in order to identify optimal designs and parameter choices for nonlinear applications. Silicon waveguides did not benefit from graphene due to the low field overlap with the sheet whereas plasmonic waveguides, and especially the slot configuration, proved to be more promising. Especially for plasmonic waveguides, FEM-modeling of acute geometric features using curved segments ("fillets") instead of right angles, proved to be more reliable for the convergence of the integrals required for the calculation of nonlinear parameters. Lastly, we calculated the nonlinear

parameters for a low index-contrast fused-silica microfiber with the addition of a graphene monolayer in several different configurations: below the microfiber, covering the microfiber and fully wrapped around it. Based on recent experimental results related to this waveguide structure (Wu et al 2014), we have reasons to anticipate that the actual nonlinear surface conductivity of graphene might be up to three orders of magnitude higher than the one predicted in theory (Hendry et al 2010; Khurgin 2014).

Acknowledgements Alexandros Pitilakis acknowledges the support of the "IKY Fellowships of Excellence for Postgraduate Studies in Greece - Siemens Programme". This research has been co-financed by the European Union (European Social Fund–ESF) and Greek national funds through the Operational Program "Education and Lifelong Learning" of the National Strategic Reference Framework (NSRF): Research Funding Program THALES (Project ANEMOS).

References

Afshar Vahid S, Monro TM (2009) A full vectorial model for pulse propagation in emerging waveguides with subwavelength structures part i: Kerr nonlinearity. Opt Express 17(4):2298–2318

Agrawal GP (2007) Nonlinear Fiber Optics, 4th edn. Academic Press, U.S.A.

Bao Q, Zhang H, Wang B, Ni Z, Lim CHYX, Wang Y, Tang DY, Loh KP (2011) Broadband graphene polarizer. Nat Photonics 5(7):411–415

Bludov YV, Ferreira A, Peres NMR, Vasilevskiy MI (2013) A primer on surface plasmon-polaritons in graphene. Int J Mod Phys B 27(10):1341,001

Boardman A, King N, Rapoport Y (2007) Metamaterials driven by gain and special configurations. In: Proceedings of SPIE, vol 6581, p 658108

Boyd R (2008) Nonlinear Optics. Elsevier Science

Butcher P, Cotter D (eds) (1990) The Elements of Nonlinear Optics. Cambridge University Press, Great Britain

Chatzidimitriou D, Pitilakis A, Kriezis EE (2015) Rigorous calculation of nonlinear parameters in graphene-comprising waveguides. J Appl Phys 118(2):023,105

Cheng JL, Vermeulen N, Sipe JE (2014) Third order optical nonlinearity of graphene. New J Phys 16(5):053,014

Collin RE (1990) Field Theory of Guided Waves, 2nd edn. Wiley-IEEE Press

Daniel BA, Agrawal GP (2010) Vectorial nonlinear propagation in silicon nanowire waveguides: Polarization effects. J Opt Soc Am B 27(5):956–965

Falkovsky LA (2008) Optical properties of graphene and iv-vi semiconductors. Phys Usp 178(9):923

Geim A, Novoselov K (2007) The rise of graphene. Nat Mater 6(3):183–191

Gu T, Petrone N, McMillan JF, van der Zande a, Yu M, Lo GQ, Kwong DL, Hone J, Wong CW (2012) Regenerative oscillation and four-wave mixing in graphene optoelectronics. Nat Photonics 6(8):554–559

Hanson G (2008) Dyadic green's functions for an anisotropic, non-local model of biased graphene. IEEE Trans Antennas Propag 56(3):747–757

Hendry E, Hale PJ, Moger J, Savchenko AK, Mikhailov SA (2010) Coherent nonlinear optical response of graphene. Phys Rev Lett 105(9):097,401

Jablan M, Buljan H, Soljačić M (2009) Plasmonics in graphene at infrared frequencies. Phys Rev B 80(24):245,435

Khurgin JB (2014) Graphene - a rather ordinary nonlinear optical material. Appl Phys Lett 104(16):161,116

Koos C, Jacome L, Poulton C, Leuthold J, Freude W (2007) Nonlinear silicon-on-insulator waveguides for all-optical signal processing. Opt Express 15(10):5976–5990

Leon-Saval S, Birks T, Wadsworth W, Russell PSJ, Mason M (2004) Supercontinuum generation in submicron fibre waveguides. Opt Express 12(13):2864–2869

Liu M, Yin X, Ulin-Avila E, Geng B, Zentgraf T, Ju L, Wang F, Zhang X (2011) A graphene-based broadband optical modulator. Nature 474(7349):64–7

Liu M, Yin X, Zhang X (2012) Double-layer graphene optical modulator. Nano Lett 12(3):1482–5

Midrio M, Galli P, Romagnoli M, Kimerling LC, Michel J (2014) Graphene-based optical phase modulation of waveguide transverse electric modes. Photonics Res 2(3):A34

Mikhailov SA, Ziegler K (2008) Nonlinear electromagnetic response of graphene: frequency multiplication and the self-consistent-field effects. J Phys: Condens Matter 20(38):384,204

Nikitin AY, Guinea F, García-Vidal FJ, Martín-Moreno L (2011) Edge and waveguide terahertz surface plasmon modes in graphene microribbons. Phys Rev B 84(16):161,407

Novoselov K, Fal'Ko V, Colombo L, Gellert P, Schwab M, Kim K (2012) A roadmap for graphene. Nature 490(7419):192–200

Onural L (2006) Impulse functions over curves and surfaces and their applications to diffraction. Journal of Mathematical Analysis and Applications 322(1):18 – 27

Otsuji T, Tombet SAB, Satou A, Fukidome H, Suemitsu M, Sano E, Popov V, Ryzhii M, Ryzhii V (2012) Graphene-based devices in terahertz science and technology. J Phys D: Appl Phys 45(30):303,001

Pitilakis A, Kriezis EE (2013) Highly nonlinear hybrid silicon-plasmonic waveguides: Analysis and optimization. J Opt Soc Am B 30(7):1954–1965

Pitilakis A, Chatzidimitriou D, Kriezis EE (2015) A strict framework for analyzing linear and nonlinear propagation in photonic and terahertz graphene waveguides. In: Transparent Optical Networks (ICTON), 2015 17th International Conference on, Budapest, Hungary, pp 1–4

Rapoport Y (2014) General method for the derivations of the evolution equations and modeling nonlinear waves in active layered structures with surface and volume nonlinearities. In: Bulletin of Taras Shevchenko National University of Kyiv, Series Physics & Mathematics, 1, pp 281–288,

`http://www.library.univ.kiev.ua/ukr/host/10.23.10.100/db/ftp/visnyk/fiz_mat_1_2014.pdf`

Rapoport Y, Grimalsky V (2011) Nonlinear surface 2D plasmons and giant second harmonic generation. In: Proceedings of the International Conference Days on Diffraction (DD 2011), 6094387, pp 168–173

Snyder AW, Love JD (1983) Optical Waveguide Theory. Chapman and Hall, U.S.A.

Stauber T, Peres N, Geim A (2008) Optical conductivity of graphene in the visible region of the spectrum. Phys Rev B 78(8):085,432

Sun Z, Hasan T, Torrisi F, Popa D, Privitera G, Wang F, Bonaccorso F, Basko DM, Ferrari AC (2010) Graphene mode-locked ultrafast laser. ACS Nano 4(2):803–810

Vakil A, Engheta N (2011) Transformation optics using graphene. Science 332(6035):1291–4

Volakis J, Chatterjee A, Kempel L (1998) Finite element method for electromagnetics. IEEE Press

Wu Y, Yao B, Cheng Y, Rao Y, Gong Y, Zhou X, Wu B, Chiang KS (2014) Four-wave mixing in a microfiber attached onto a graphene film. IEEE Photonics Technol Lett 26(3):249–252

Xia F, Mueller T, Lin YM, Valdes-Garcia A, Avouris P (2009) Ultrafast graphene photodetector. Nat Nanotechnol 4(12):839–43

Xia F, Wang H, Xiao D, Dubey M, Ramasubramaniam A (2014) Two-dimensional material nanophotonics. Nat Photon 8(12):899–907

Zhang H, Virally S, Bao Q, Ping LK, Massar S, Godbout N, Kockaert P (2012) Z -scan measurement of the nonlinear refractive index of graphene. Opt Lett 37(11):1856–1858